Precision Control Method and Experimental Validation of Axial Shortening in Inertial Friction Welding Based on Single-Neuron Adaptive PID Strategy

Zhike Qu , Jie Yang * , Chunming Xia , Yingfan Ren , Run Gu , Xiaowei Wang

Posted Date: 31 March 2026

doi: 10.20944/preprints202603.2362.v1

Keywords: inertial friction welding; valve-controlled hydraulic motor; single-neuron PID; axial shortening

 doi:10.20944/preprints202603.2362.v1

Article

Precision Control Method and Experimental Validation of Axial Shortening in Inertial Friction Welding Based on Single-Neuron Adaptive PID Strategy

Zhike Qu [1], Jie Yang [1,2,*],Chunming Xia [1], Yingfan Ren [1], Run Gu [1] and Xiaowei Wang [1]

[1] School of Mechanical and Automotive Engineering, Shanghai University of Engineering Science, Shanghai 201620

[2] Shanghai Collaborative lnnovation Center of Intelligent Manufacturing Robot Technology for Large Components, Shanghai 201620

* Correspondence: j.yang@sues.edu.cn

Abstract

Addressing the critical challenge of precision control over axial shortening in inertial friction welding, this paper proposes an intelligent control method based on a valve-controlled hydraulic motor system. By establishing an accurate transfer function model of the system, two controllers—conventional PID and single-neuron adaptive PID—were designed, and a co-simulation platform integrating AMESim and Simulink was employed for collaborative validation of the hydraulic system and control algorithms. Simulation results demonstrate that the single-neuron adaptive PID controller significantly outperforms conventional PID in dynamic response speed, overshoot suppression, and steady-state accuracy. To validate the practical efficacy of the control strategy, welding experiments were conducted with a target axial shortening value at 400 rpm, and precision testing was performed under extreme conditions by increasing the initial welding speed to 420 rpm. Experimental results indicate a minimal axial shortening deviation of only 0.16 mm between the preset and target speeds, confirming the proposed method's exceptional robustness and engineering applicability for precision axial shortening control. This study provides a theoretical foundation and technical pathway for intelligent control of high-performance inertial friction welding equipment.

Keywords: inertial friction welding; valve-controlled hydraulic motor; single-neuron PID; axial shortening

1. Introduction

Inertial friction welding (IFW) [1–4] is an advanced solid-state joining technique that employs inertial forces to generate interfacial friction, thereby producing frictional heat and inducing plastic deformation of workpieces to achieve metallurgical bonding. In aero-engine integrated structures, welded components must adhere to stringent length tolerances dictated by operational conditions. Consequently, precise regulation of axial shortening during the welding process is imperative—not only to ensure dimensional compliance but also to streamline post-weld machining and enable sequential multi-stage welding operations.

Numerous scholars have conducted research on the inertial friction welding (IFW) of FGH96 superalloy [5–8]. Zhang Lu and Zhang Chunbo et al. [9,10] performed process experiments on GH4169/FGH96 dissimilar alloy joints (φ145×6.5mm) using the HWI-IFW-130 friction welding machine developed by the Harbin Welding Research Institute, achieving high-performance welded joints and pioneering new approaches for large-scale annular component IFW processes.Yang Jun et

 doi:10.20944/preprints202603.2362.v1

al. [11] investigated the effects of welding parameter variations on the microstructure and high-temperature tensile properties of FGH96 powder metallurgy superalloy joints during IFW.Additional studies have focused on control strategies for IFW systems [12–14].To address the insufficient control precision of conventional friction welding hydraulic systems, Zhang Chunbo et al. [15] proposed a hybrid open-loop/closed-loop control method. Experimental results demonstrated its effectiveness in coordinating force control requirements across different welding phases, with the closed-loop mode significantly improving joint quality. Du Suigeng et al.[16,17]developed a computer-controlled closed-loop system based on electro-hydraulic proportional valves, achieving superior performance metrics including 2.17% linearity, 2% control accuracy, and 1.4Hz bandwidth outperforming traditional electro-hydraulic servo systems.

This research implements a proportional valve-regulated hydraulic motor system for inertial friction welding equipment. Through rigorous theoretical analysis, a transfer function model of the system was derived. An integrated co-simulation platform combining AMESim and Simulink was developed to construct a comprehensive simulation model of the proportional valve-controlled hydraulic motor system. Comparative simulation studies were conducted employing two distinct control strategies: conventional PID and single-neuron adaptive PID control.For experimental verification, welding trials were performed with a target axial shortening measurement at 400rpm. The initial welding velocity was elevated to 420rpm to assess control efficacy. System performance was validated by analyzing the axial shortening differential between the 420rpm and 400rpm operational regimes.

2. Mathematical Modeling of Proportional Valve-Controlled Hydraulic Motor System

As illustrated in Figure 1, the proportional valve-regulated hydraulic motor system comprises a hydraulic power unit, proportional directional valve, control unit, proportional amplifier, flow control valve, and hydraulic motor. The hydraulic power unit functions as the system's primary drive mechanism. Integrated feedback sensors perpetually acquire and transmit operational parameters from the hydraulic motor to the controller.The control unit processes these feedback signals and generates corresponding command outputs to the proportional amplifier. These amplified control signals subsequently actuate both the proportional directional valve and flow control valve. The proportional valve modulates flow rate through precise spool displacement to vary the orifice cross-sectional area, while the flow control valve governs flow velocity and pressure differential. This synchronized operation enables precise regulation of the hydraulic motor's rotational velocity.

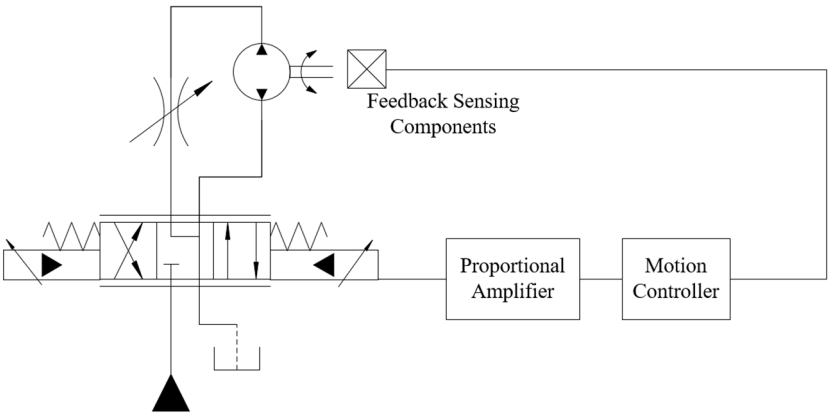

Figure 1. Schematic diagram of the proportional valve-controlled hydraulic system.

Figure 2 illustrates the schematic diagram of the hydraulic motor and proportional valve components within the proportional valve-controlled motor system, where the key parameters are defined as follows: B_m is the viscous damping coefficient of the hydraulic motor and load , T_L is the

 doi:10.20944/preprints202603.2362.v1

external load torque applied to the motor shaft, θ_m is the angular displacement of the hydraulic motor (rad), J_t is the total equivalent moment of inertia referred to the motor shaft .

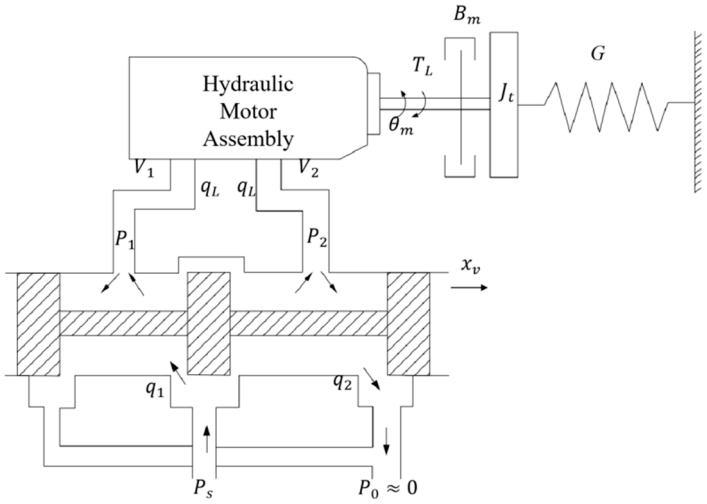

Figure 2. Schematic diagram of a proportional valve-regulated hydraulic motor.

According to the relationship between mechanisms in the automatic transmission and control section of the hydraulic system, as well as the requirements of system dynamics, the mathematical models of the proportional valve and hydraulic motor can be derived as follows.

By performing Taylor series expansion of the original equation at a certain point and neglecting higher-order infinitesimal terms as follows:

$$q_L - q_{LA} = \frac{\partial q_L}{\partial x_v}\Delta x_v + \frac{\partial q_L}{\partial P_L}\Delta P_L + \frac{\partial q_L}{\partial P_s}\Delta P_s \tag{1}$$

The Laplace transform of the valve load flow equation is given as follows:

$$q_L(s) = K_q x_v(s) - K_c P_L(s) \tag{2}$$

The flow continuity equation for the hydraulic motor is expressed as follows:

$$q_L = D_m \frac{d\theta_m}{dt} + C_{im}(P_1 - P_2) + \frac{1}{2}C_{em}(P_1 - P_2) + \frac{V_1}{2\beta_e}\left(V_{01}\frac{dP_1}{dt} - V_{02}\frac{dP_2}{dt}\right) \tag{3}$$

The Laplace transform of the flow continuity equation can be expressed as follows:

$$q_L(s) = D_m s d\theta_m(s) + \left(C_{nm} + \frac{V_t}{4\beta_e}s\right)P_L(s) \tag{4}$$

Based on the principle of torque balance, the equilibrium relationship between the hydraulic motor output torque and the aforementioned load torque can be represented as follows:

$$D_m P_L = J_t \frac{d^2\theta_m}{dt^2} + B_m \frac{d\theta_m}{dt} + G\theta_m + T_L \tag{5}$$

The Laplace transform of Equation (1-5) yields as follows:

$$D_m P_L(s) = \theta_m(s)\left(J_t s^2 + B_m s + G\right) + T_L(s) \tag{6}$$

By simultaneously solving Equations (2), (4), and (6) to eliminate intermediate variables as:

 doi:10.20944/preprints202603.2362.v1

$$\theta_m(s)=\frac{\frac{K_q}{D_m}x_v(s)-\frac{K_{ce}}{D_m^2}(1+\frac{V_t}{4\beta_e K_{ce}}s)T_L(s)}{(\frac{s^2}{\omega_m^2}+\frac{2\xi ms}{\omega_m}+1)s} \tag{7}$$

The transfer function of the hydraulic motor can be expressed as follows:

$$\omega(s)=\frac{\frac{K_q}{D_m}x_v(s)-\frac{K_{ce}}{D_m^2}\left(1+\frac{V_t}{4\beta_e K_{ce}}s\right)T_L(s)}{\frac{s^2}{\omega_m^2}+\frac{2\xi_m s}{\omega_m}+1} \tag{8}$$

The mathematical model of the proportional amplifier is given as follows:

$$G_a(s)=\frac{I(s)}{U(S)}=K_a \tag{9}$$

The transfer function of the sensing and feedback element is expressed as follows:

$$G_f(s)=\frac{U_f(s)}{\omega(s)}=K_f \tag{10}$$

The transfer function of the proportional valve is given as follows:

$$G_v(s)=\frac{x_v(s)}{I(s)}=\frac{K_v}{\frac{s^2}{\omega_v^2}+\frac{2\xi_v s}{\omega_v}+1} \tag{11}$$

Based on the transfer functions established for each component in the aforementioned system, and in accordance with the configuration and operational principles of the proportional valve-controlled motor system, the complete block diagram of the system transfer function is derived as shown in Figure 3.

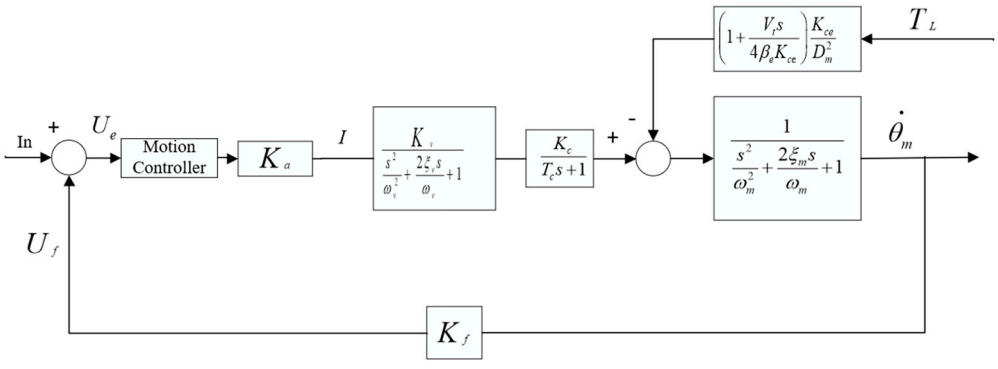

Figure 3. Block diagram of the transfer function of a valve-regulated hydraulic motor system.

The transfer function of the valve-controlled hydraulic motor system is derived from Figure 1-3 and expressed as follows:

$$G(s)=\frac{U_f(s)}{U_e(s)}=\frac{K_{sys}}{\left(\frac{s^2}{\omega_v^2}+\frac{2\xi_v s}{\omega_v}+1\right)\left(\frac{s^2}{\omega_m^2}+\frac{2\xi_m s}{\omega_m}+1\right)} \tag{12}$$

 doi:10.20944/preprints202603.2362.v1

In the modeling process of the proportional valve-controlled hydraulic motor system, key components including hydraulic motors, oil pumps, and tanks were selected from the hydraulic library of the AMESim simulation platform based on the system architecture. Following the established schematic diagram, compatible submodels were chosen and parameterized, ultimately forming the AMESim simulation model of the valve-controlled hydraulic motor system as illustrated in Figure 4. The primary parameters involved in this model are summarized in Table 1.

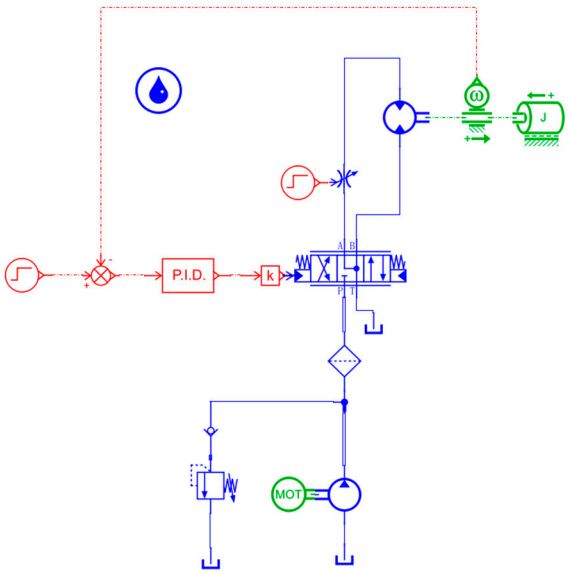

Figure 4. AMESim simulation model of a valve-controlled hydraulic motor.

Table 1. Parameter settings of the valve-controlled motor system.

Parameter Name	Parameter Value	Units
Hydraulic motor displacement	4.46×10^{-6}	m^3/rad
Load moment of inertia	7.25×10^{-3}	$kg\cdot m^2$
Valve flow-pressure coefficient	1.33×10^{-12}	$m^5/(N\cdot s)$
Motor total leakage coefficient	7.00×10^{-13}	$m^5/(N\cdot s)$
Total flow-pressure coefficient	2.03×10^{-12}	$m^5/(N\cdot s)$
Total enclosed volume	3.90×10^{-4}	m^3
Effective bulk modulus	7.00×10^{8}	Pa

3. Controller Design and Simulation

3.1. PID Control

The system architecture of the classical PID control algorithm is illustrated in Figure 5.

 doi:10.20944/preprints202603.2362.v1

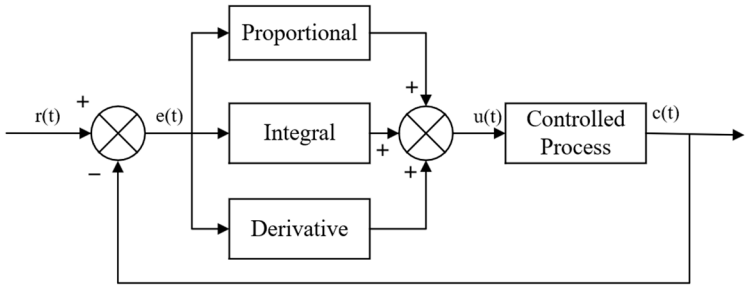

Figure 5. Schematic diagram of the PID control system.

The control law of the PID controller is given as follows :

$$u(t) = K_p(e(t) + \frac{1}{T_t}\int_0^t e(t)dt + T_D\frac{de(t)}{dt}) \quad (13)$$

Figure 6 demonstrates the PID control simulation model constructed within the MATLAB/Simulink simulation platform.

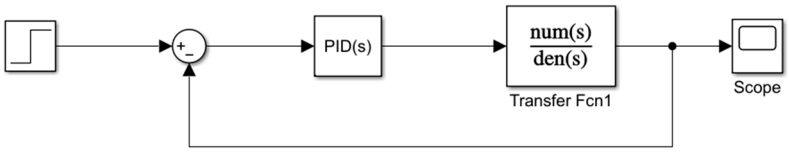

Figure 6. PID simulation model in Simulink.

During the PID parameter tuning process, initial controller parameters are first established, followed by meticulous adjustments based on the influence of each parameter on the system's dynamic characteristics, ultimately achieving optimal response output. Experimental validation yielded the final PID controller parameters as follows: $K_p = 20,\ K_i = 2,\ K_d = 0.01$ .The simulation employed a unit step input (amplitude = 1) with a 10-second duration, with results presented in Figure 7. The simulation reveals a pronounced dynamic response overshoot of 30%, a rise time of 0.8 seconds, and a settling time of 2.3 seconds to reach steady-state conditions.

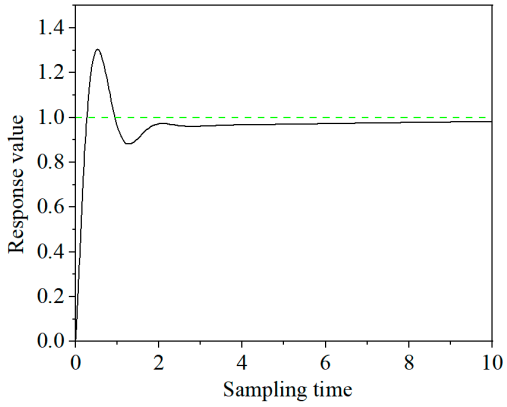

Figure 7. PID simulation graph.

 doi:10.20944/preprints202603.2362.v1

3.2. Single-Neuron PID Control

The mathematical model of the single neuron is illustrated in Figure 8.

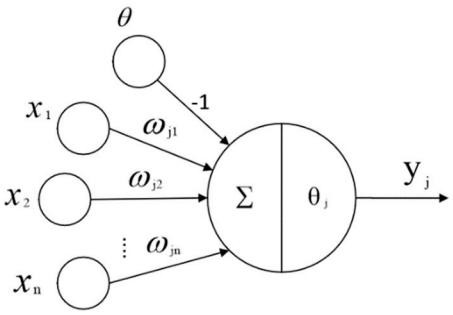

Figure 8. Single neuron model.

The output value derived from the single-neuron model is expressed as follows:

$$y_j = \sum_{i=1}^{n} \omega_{ji} X_i - \theta_j \tag{14}$$

The learning mechanism of single neurons primarily incorporates unsupervised Hebb rules, supervised Delta rules, and their hybrid variants. The unsupervised Hebb learning follows the principle of neuronal co-activation, where the synaptic weight increment between simultaneously activated adjacent neurons exhibits positive correlation with the product of their output responses. Given the activation states of neurons i and j as O_i、O_j, the weight update mechanism follow:

$$\Delta\omega_{ij}(k) = \eta O_j(k) O_i(k) \tag{15}$$

The supervised Delta learning mechanism incorporates error signals into the Hebb framework, substituting the original output term with the difference between desired and actual outputs. The corresponding weight adjustment formula is given as follows:

$$\Delta\omega_{ij}(k) = \eta(d_j(k) - O_j(k)) O_i(k) \tag{16}$$

Supervised Hebb learning synthesizes these dual mechanisms into a composite weight update strategy, formally expressed as follows:

$$\Delta\omega_{ij}(k) = \eta(d_j(k) - O_j(k)) O_j(k) O_i(k) \tag{17}$$

The single-neuron adaptive controller dynamically adjusts weighting coefficients through this supervised Hebb learning framework, achieving self-organizing system optimization. The core control algorithm and learning strategy are formulated as follows:

$$u(k) = u(k-1) + K\sum_{i=1}^{3} \omega_i'(k) x_i(k) \tag{18}$$

$$\omega_i'(k) = \frac{\omega_i(k)}{\sum_{i=1}^{3} |\omega_i(k)|} \tag{19}$$

$$\omega_1(k) = \omega_1(k-1) + \eta_P z(k) u(k) x_1(k) \tag{20}$$

 doi:10.20944/preprints202603.2362.v1

$$\omega_2(k)=\omega_2(k-1)+\eta_I z(k)u(k)x_2(k) \quad (21)$$

$$\omega_3(k)=\omega_3(k-1)+\eta_D z(k)u(k)x_3(k) \quad (22)$$

The single-neuron based control architecture is illustrated in Figure 9.

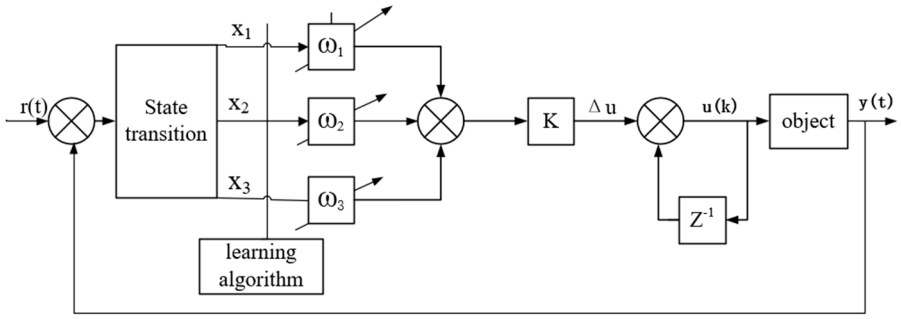

Figure 9. Block diagram of single neuron PID control.

The system simulation model, developed within MATLAB's Simulink environment, implements the single-neuron PID control algorithm as structurally depicted in Figure 10.

Figure 10. Single neuron PID simulation model.

Figure 11 presents the subroutine architecture of the single-neuron PID controller.

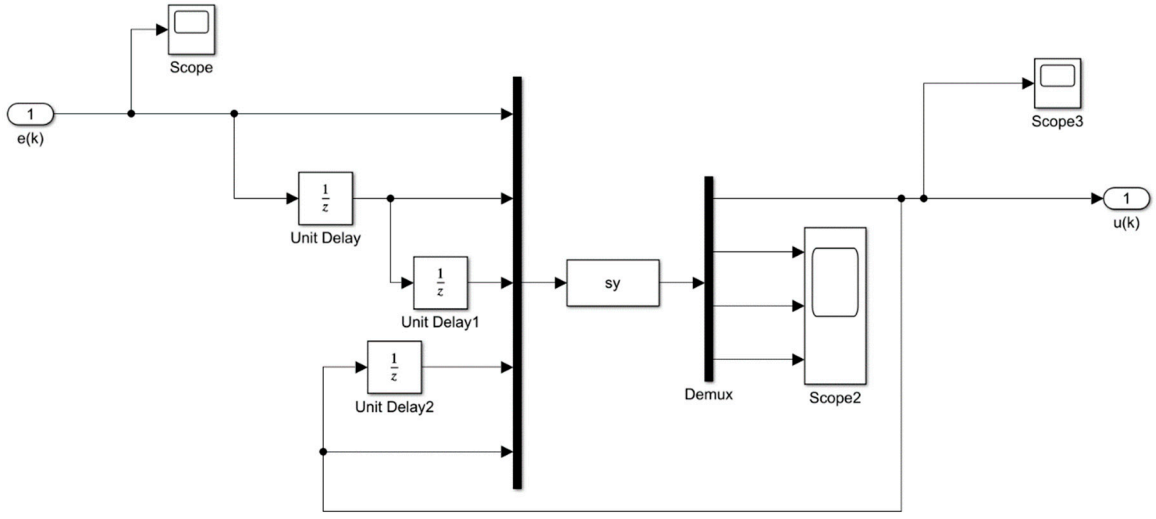

Figure 11. Single neuron PID controller.

 doi:10.20944/preprints202603.2362.v1

Figure 12 presents the simulation results of the single-neuron PID control system. Under test conditions employing a unit step input (amplitude = 1) with 10-second simulation duration, the system demonstrates 17% overshoot, achieves a rise time of 0.75 seconds, and attains steady-state conditions within 1.8 seconds.

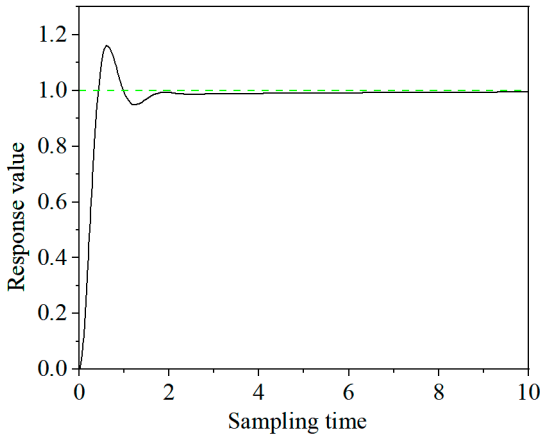

Figure 12. Single neuron PID simulation graph.

A comparative simulation study was conducted to evaluate the performance characteristics of conventional PID versus single-neuron PID control. Figure 13 illustrates the dynamic response comparison, while Table 2 provides quantitative performance metrics under step-input conditions.

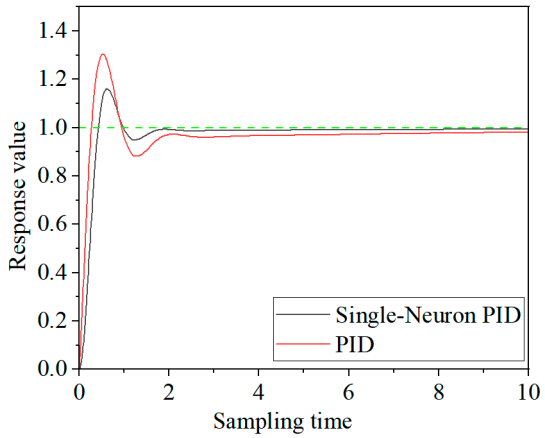

Figure 13. Comparison of PID and single neuron PID simulations.

Table 2. Simulation data of two controllers.

Control Algorithm	Rise Time (s)	Settling Time (s)	Overshoot (%)
Classical PID	0.8	2.3	30%
Single-Neuron PID	0.75	1.8	17%

Table 2 demonstrates that the conventional PID control algorithm exhibits significantly greater overshoot and longer settling time compared to the single-neuron PID approach, with merely a 0.05s difference in rise time. Moreover, while conventional PID control shows substantial steady-state deviation from the desired step response, the single-neuron variant achieves markedly superior setpoint tracking accuracy.In inertial friction welding systems, reduced settling time facilitates earlier

 doi:10.20944/preprints202603.2362.v1

stabilization of hydraulic motor speed, thereby enhancing axial shortening control precision. Excessive overshoot during actual welding operations directly compromises axial shortening accuracy, subsequently impairing weld formation quality through adverse effects on plastic deformation dynamics and forging pressure consistency.

4. Experimental Validation

As illustrated in Figure 14, the axial shortening in inertial friction welding exhibits a positive correlation with energy input during the welding process. Given constant system rotational inertia, the initial rotational speed of the welding machine predominantly determines the energy input. Consequently, precise control of axial shortening necessitates regulation of the rotational speed throughout the welding operation.

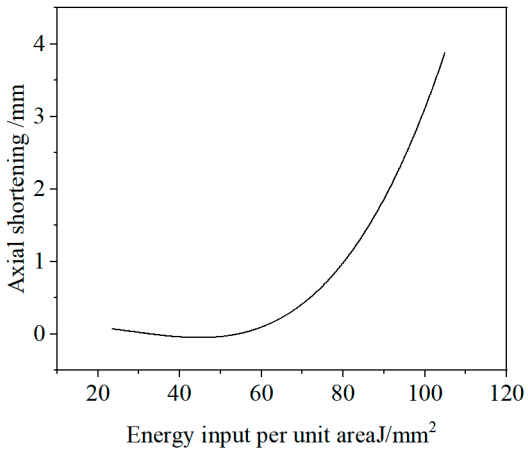

Figure 14. The relationship between the energy input and the amount of axial shortening.

4.1. Hardware Design and Selection of Inertial Friction Welding Machine

Figure 15 illustrates the closed-loop control architecture of the system. A speed sensing unit continuously monitors the rotational speed of the hydraulic motor and converts it into a 0–10 V voltage signal via a signal conditioning circuit. This signal is then acquired through the analog input channel of the PLC. The main control unit of the PLC applies digital filtering to the raw data and dynamically compares it with preset speed reference values to compute real-time speed deviations. Correction parameters, calculated using a PID algorithm, are transmitted via an industrial bus to the CNC system. During welding operations, the CNC system dynamically responds to control commands from the PLC, precisely adjusting the drive signals of the hydraulic motor to achieve closed-loop control of the welding speed.

 doi:10.20944/preprints202603.2362.v1

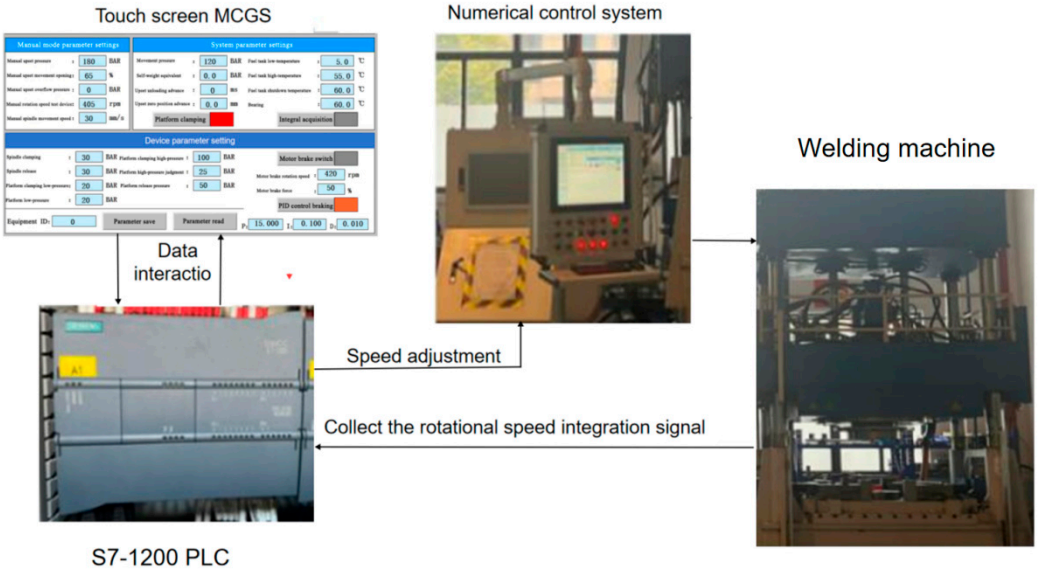

Figure 15. Schematic diagram of closed-loop control structure of friction wadding machine.

Given the system's requirements for industrial bus communication interface expansion and integration with a physical control panel, there is a significant demand for digital interface resources. To accommodate multi-channel analog signal acquisition—such as for rotational speed and pressure parameters—as well as actuator drive functions, the main control unit must incorporate an AD/DA conversion module with excellent human-machine interaction capabilities. After a comprehensive evaluation of the equipment control requirements, this study selected the Siemens S7-1200PLC as the control core, as shown in Figure 16. The S7-1200PLC is characterized by its compact design, high level of integration, and high-speed processing capability, with an instruction processing speed of 0.065 microseconds per instruction. The base unit is equipped with 24 digital input/output channels. Through expandable analog input modules, it supports four-channel synchronous acquisition of dynamic welding parameters. When combined with analog output modules, it enables precise transmission of control signals.

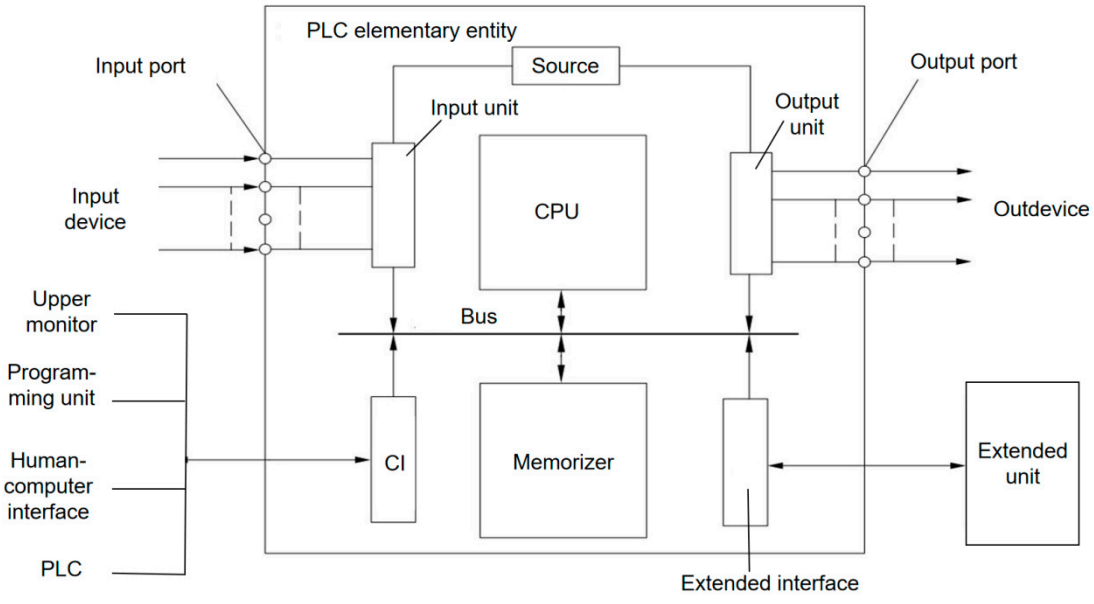

Figure 16. Block diagram of S7-1200 PLC composition.

 doi:10.20944/preprints202603.2362.v1

The system employs Kunlong Tongtai industrial touchscreens as the upper computer interface terminals. These touchscreens feature dual serial communication interfaces (RS232/RS485), enabling seamless data exchange with the PLC via the Modbus protocol. They support tilt installation within the range of 0°~30° and have an operating temperature threshold below 45°C. The HMI integrates an intuitive interface and user-friendly development software (e.g., Kinco HMIware), supporting multiple programming languages and scripting capabilities, which significantly enhances system development flexibility. Notably, the HMI exhibits broad compatibility with various PLCs, servo drives, and industrial equipment, and supports mainstream communication protocols including Modbus, CANopen, and Profibus. It also provides comprehensive display and operational functionalities.

For rotational speed measurement of the hydraulic motor in the inertial friction welding machine, the Ailiewei ESHF11018 sensor is utilized. This specialized hydraulic motor sensor detects changes in magnetic flux density when ferromagnetic materials approach the probe. The Hall IC senses these variations, and the backend circuitry converts them into pulse outputs proportional to the rotational speed of the gear. The sensor features a wide frequency response, fast response time, long mechanical lifespan, high stability, and robust durability. Table 3 summarizes the sensor's performance parameters, and its physical dimensions are illustrated in Figure 17.

Table 3. Speed sensor parameters.

Technical Specifications	Parameter Values
Frequency range	0~5KHz
Power supply voltage	4.5~20VDS
Output current	7mA±20%/14mA±20%
Sensitivity	2.0±0.1mv/v

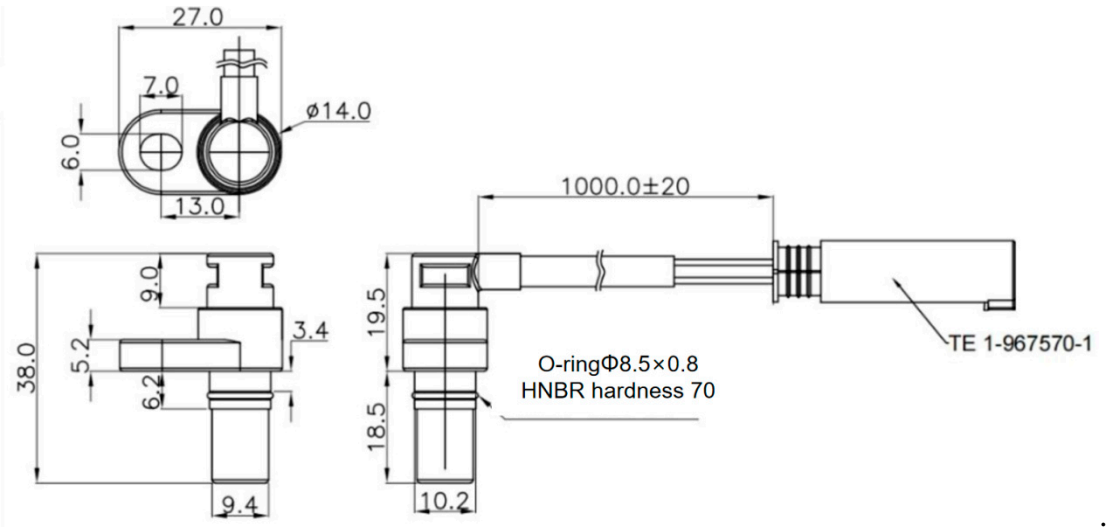

Figure 17. Dimensional drawing of the speed sensor.

4.2. PLC Software Design

This paper presents a valve-controlled hydraulic motor system design that achieves axial shortening control through precise regulation of the motor's rotational speed during welding. The methodology establishes the integral value of the rotational speed decay curve under target conditions as the control reference, which quantitatively represents the cumulative energy input throughout the welding process.During operation, speed sensors continuously monitor the hydraulic

 doi:10.20944/preprints202603.2362.v1

motor's rotational velocity, transmitting real-time data to a PLC system. The embedded PID controller processes these measurements, performing instantaneous integration to calculate the current cumulative speed value. This integrated parameter undergoes continuous comparison with the predetermined target integral.When the instantaneous integral exceeds the target value - indicating either insufficient speed decay or excessive rotational velocity,the PID controller generates corrective signals to accelerate speed reduction. Equilibrium is achieved when the real-time integral matches the target value, signifying equivalent energy output to the reference condition and, consequently, identical axial shortening. The corresponding control flowchart is presented in Figure 18.

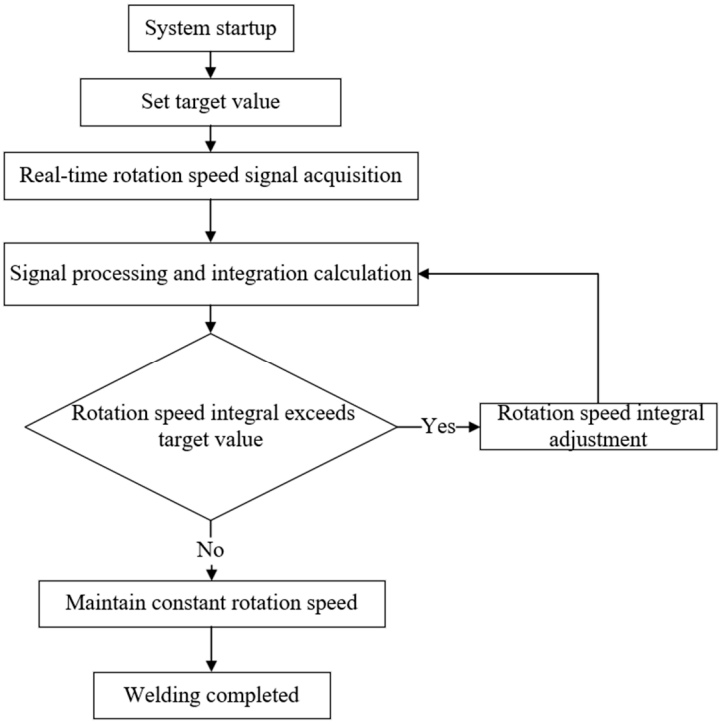

Figure 18. Flow chart of hydraulic motor speed control.

The speed integral acquisition process operates in two distinct modes: idle operation and active welding. During idle operation (manual mode), the system evaluates multiple PID parameter sets through rotational speed integral collection to identify optimal control parameters. This preparatory phase minimizes both parameter adjustment time and material waste during actual welding trials.In active welding (automatic mode), the system implements pre-optimized welding parameters while continuously acquiring speed integral data at 20ms intervals. Acquisition terminates upon spindle rotation cessation, with the collected integral serving as the control reference value.

Prior to conducting actual welding experiments, preliminary idle-run simulations were performed to optimize the PID parameters. As evidenced by the rotational speed control curves under various PID configurations presented in Figure 19, the parameter set (P=15, I=0.1, D=0.01) demonstrated superior performance characteristics.

 doi:10.20944/preprints202603.2362.v1

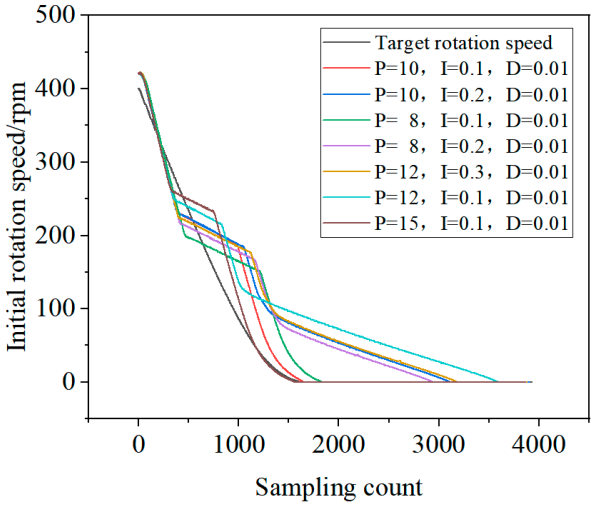

Figure 19. Speed curves under different PID parameters.

As illustrated in Figure 20, the parameter input interface during welding operation is shown. The optimized welding parameters (initial rotational speed and friction pressure) are first input into the system, with the speed integral acquisition function activated to initiate the welding process. Upon completion, the speed integral obtained at this initial rotational speed serves as the target reference value for subsequent PID control, while the resulting axial shortening constitutes the ultimate control objective.Adjusting the initial welding speed to 420 rpm while maintaining other operational parameters ,deactivating the speed integral acquisition function,engaging the PID-controlled braking system,implementing the predetermined PID parameter values (P=15, I=0.1, D=0.01).

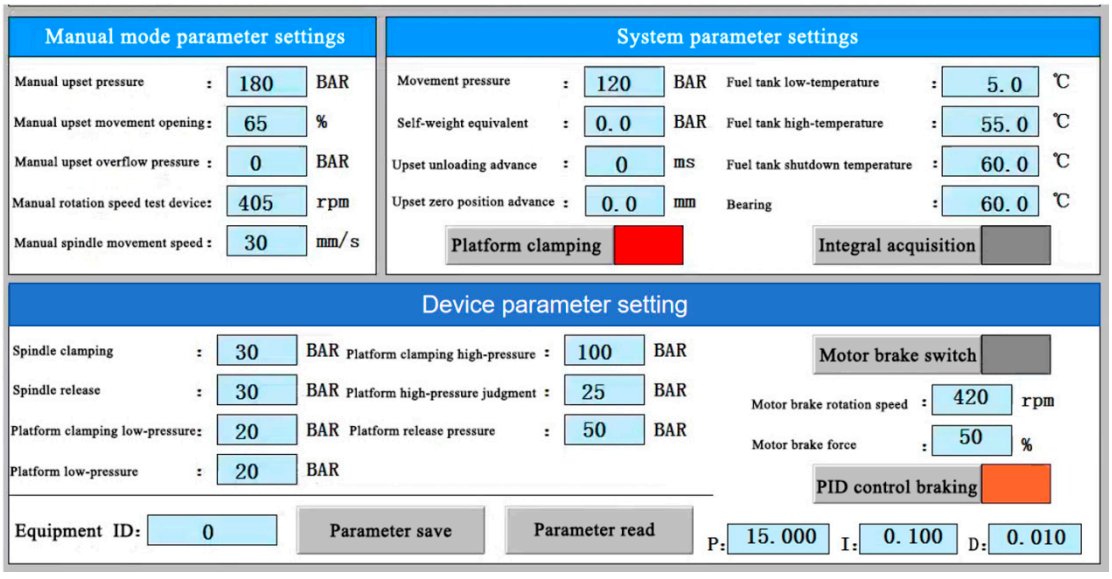

Figure 20. Welding machine parameter settings.

As shown in Figure 21, the comparative analysis between the target speed decay curve and the controlled speed decay profile reveals several important findings. When the sampling count reaches 100 points, corresponding to a welding duration of 2 seconds, the integrated speed value of the controlled process exceeds the target reference, prompting the PID controller to initiate corrective action by rapidly reducing the hydraulic motor's output speed. This intervention continues until the

 doi:10.20944/preprints202603.2362.v1

integrated speed value falls below the target threshold, at which point the controlled speed profile begins to closely follow the target decay curve until welding cessation. Figure 22 presents the axial shortening characteristics under both the target and controlled speed conditions. The experimental data demonstrates that the higher initial speed setting of 420 rpm results in significantly greater energy input compared to the target condition, causing the axial shortening curve for the controlled process to remain consistently above the target profile throughout most of the welding duration. However, through precise PID-mediated speed regulation, the system effectively reduces energy input over time, enabling the controlled axial shortening curve to gradually converge toward the target profile. The final measurements show an exceptionally small deviation of merely 0.16 mm between the controlled and target axial shortening values. These results provide conclusive evidence that the developed control system achieves highly effective regulation of welding speed while successfully maintaining axial shortening within the desired tolerances, thereby validating the proposed control methodology.

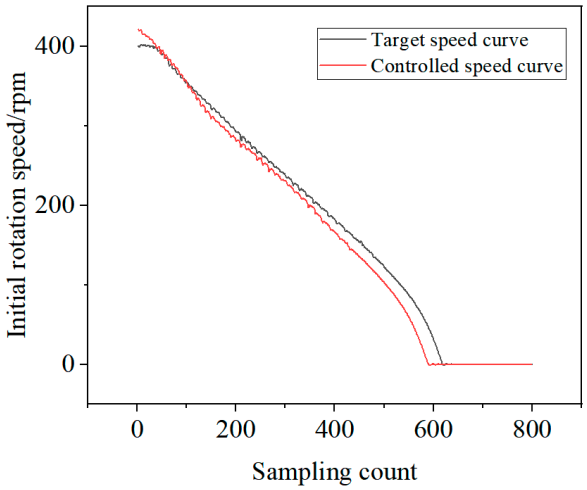

Figure 21. Target speed and set speed decay curves.

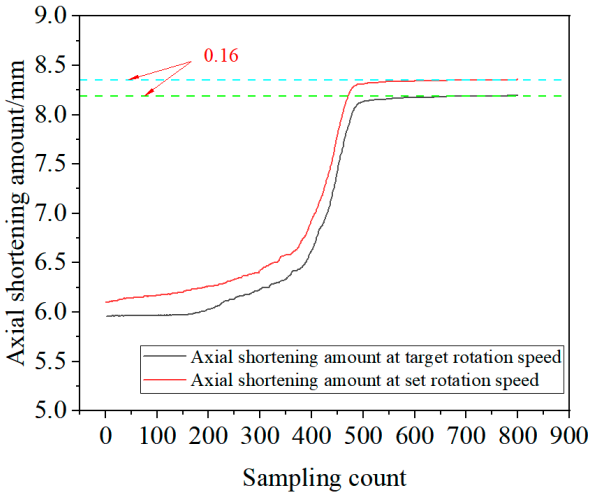

Figure 22. Axial shortening under target speed and set speed.

5. Conclusions

 doi:10.20944/preprints202603.2362.v1

(1) The hydraulic motor system was mathematically modeled by establishing the load flow equation, flow continuity equation, and force balance equation. Through simultaneous solution of these equations, the transfer function of the hydraulic motor was derived. By integrating transfer function models of key system components including the proportional valve, throttle valve, and detection sensors, the complete system transfer function was constructed. Analysis of the system transfer function yielded the following conclusions:①In the proportional valve-hydraulic motor system, the natural frequency and damping ratio are critical parameters determining dynamic performance. The natural frequency directly characterizes system responsiveness, with higher values indicating faster dynamic response. The hydraulic natural frequency primarily depends on the following parameters: load inertia on the motor output shaft, total system volume, hydraulic motor displacement, and effective bulk modulus of the system. To enhance system response speed, these parameters can be optimized accordingly.② The system gain parameter significantly influences dynamic characteristics and control precision. Increasing the gain improves the system's response frequency.③ Under constant load torque, spool displacement serves as the primary influencing factor for rotational speed control.

(2)Using Simulink, both conventional PID and single-neuron PID control algorithms were designed and implemented in corresponding controllers. Simulation results demonstrated that the single-neuron PID controller exhibits shorter settling time and reduced overshoot compared to conventional PID control.

(3)Experimental validation was conducted using the initial speed integral during welding as the target reference value for controlling axial shortening in inertial friction welding. Test results showed a minimal deviation of only 0.16mm between the axial shortening under controlled speed conditions and the target value, confirming the validity of the speed-based axial shortening control method and demonstrating the system's excellent control capability.

Author Contributions: All authors contributed to the study conception and design. Material preparation, data collection, and analysis were performed by Jie Yang,Chunming Xia, Yingfan Ren, Run Gu,and Xiaowei Wang. The first draft of the manuscript was written by Zhike Qu and all authors commented on previous versions of the manuscript. All authors read and approved the final manuscript.

Funding: The National Natural Science Foundation of China Youth Project (Project Name: Research on Single Tooth Equal Rake Angle Design Method for the Geometric Structure of Hourglass Worm Gear Hob Considering the Meshing Quality of Worm Pairs, Grant No. 52005317)、Artificial Intelligence Promotes Scientific Research Paradigm Reform and Empowers Discipline Leap Plan Project、Class III Peak Discipline of Shanghai—Materials Science and Engineering (High-Energy Beam Intelligent Processing and Green Manufacturing).

Conflicts of Interest: The authors declare no competing interests.

References

1. Huang W ,Li Y ,Yuan J , et al.Study on the enhanced accelerated-creep resistance and microstructural features of IN718 superalloy inertia friction welding joint containing a high entropy alloy interlayer[J].Materials Today Communications,2025,46112639-112639.
2. Yang X ,Yu X ,Xu Y , et al.Transient deformation of axial closed hydrostatic carrying system for high-end inertial friction welding based on fluid-thermal-solid interaction[J].Tribology International,2025,209110683-110683.
3. Medvedev Y A ,Galimov R V ,Pautov N A , et al.Analysis of the Characteristics of the Linear and Inertia Friction Welding Processes of Nickel Alloys[J].Journal of Machinery Manufacture and Reliability,2025,54(2):182-189.
4. Tang T ,Shi Q ,Zhou J , et al.Kissing bond defects in inertia friction welds of IN718 alloys: Experiment and prediction[J].Journal of Materials Processing Tech.,2025,338118786-118786.

 doi:10.20944/preprints202603.2362.v1

5. JIANG R ,YANG X ,CHENG M , et al.Experimental investigation and life prediction for the load spectrum with flight mission characteristics on a P/M superalloy[J].Chinese Journal of Aeronautics,2025,38(03):407-416.
6. Zhao P ,Li P ,Ding Z , et al.Microstructural characterization and mechanical properties of inertia friction welded FGH96 joints[J].Materials Today Communications,2025,42111194-111194.
7. LI B ,DING W ,ZHU Y , et al.Design and grindability assessment with cup shaped electroplated CBN wheel grinding turbine disc slots of powder metallurgy superalloy FGH96[J].Chinese Journal of Aeronautics,2024,37(09):521-534.
8. Liu Y ,Liu Y ,Zhang S , et al.Structure characterization of the oxide film on FGH96 superalloy powders with various oxidation degrees[J].International Journal of Minerals,Metallurgy and Materials,2024,31(09):2037-2047.
9. Zhang Chunbo, Zhou Jun, Zhang Lu, et al. Microstructure and mechanical properties of inertial friction welded joints between GH4169 and FGH96 superalloys [J].Transactions of the China Welding Institution, 2019, 40(06): 40-45+162-163.
10. Zhang Lu, Zhang Chunbo, Liao Zhongxiang, et al. Microstructure characteristics and texture distribution in weld zone of IN718/FGH96 inertial friction welded joint [J].Electric Welding Machine, 2022, 52(04): 8-13.
11. Yang Jun, Li Jinglong, Dong Dengke, et al. Effects of welding parameters on microstructure and high-temperature tensile properties of FGH96 inertial friction welded joints [J].Journal of Aeronautical Materials, 2019, 39(02): 33-41.
12. Aqueel A ,Kumar A Y ,Achhaibar S .Enhancing waste cooking oil biodiesel yield and characteristics through machine learning, response surface methodology, and genetic algorithms for optimal utilization in CI engines[J].International Journal of Green Energy,2024,21(6):1345-1365.
13. Ye F ,Zhang C ,Liu S , et al.Optimization of medium compositions and X-ray irradiation to enhance monacolin K production by Monascus purpureus in submerged fermentation[J].Process Biochemistry,2024,141:50-60.
14. Alardhi M S ,Salman D A ,Breig M J S ,et al.Artificial neural network and response surface methodology for modeling reverse osmosis process in wastewater treatment[J].Journal of Industrial and Engineering Chemistry,2024,133:599-613.
15. Zhang Chunbo, Zhang Yan, Wang Xu, et al. Research on friction welding technology based on interactive open-loop and closed-loop force control modes [J].Welding & Joining, 2019, (08): 53-57+68.
16. Du Suigeng, Fu Li, Yan Junhui, et al. Development of electro-hydraulic proportional computer closed-loop control system for friction welding process [J].Chinese Journal of Mechanical Engineering, 2002, (12): 135-137+141.
17. Du Suigeng, Chen Qiang, Zhu Wenchao. PLC-based closed-loop control system for friction welding process [J].Electric Welding Machine, 2009, 39(06): 53-56.